Zhu et al. *Zool. Res.* 2026, 47(2): 487−502
https://doi.org/10.24272/j.issn.2095-8137.2025.217
https://cstr.cn/32248.14.zr.2025.217

ZR | Zoological Research

Article Open Access

Multidimensional visual feature encoding and functional organization in the pigeon entopallium

Jun-Cai Zhu[1], Min-Jie Zhu[1], Qing-Zhi He[1], Peng Wu[1], Xiao-Ke Niu[1,2], Jiang-Tao Wang[1,2], Zhi-Zhong Wang[1,2,*]

[1] *School of Electrical and Information Engineering*, *Zhengzhou University*, *Zhengzhou*, *Henan* 450001, *China*

[2] *Henan Key Laboratory of Brain Science and Brain Computer Interface Technology*, *Zhengzhou*, *Henan* 450001, *China*

ABSTRACT

Understanding how birds perceive and recognize visual objects remains a fundamental question in neuroscience. The entopallium, a key node in the avian tectofugal pathway, has long been implicated in complex visual processing, yet its internal functional architecture remains incompletely understood. In this study, neuronal activity in the pigeon entopallium was systematically mapped using controlled visual stimuli that independently varied in color, shape, and motion. Recordings revealed marked hue selectivity that remained invariant across luminance levels, pronounced orientation tuning in response to shape stimuli, and robust direction selectivity for moving stimuli. Spatial mapping further revealed distinct functional segregation, with color-selective neurons localized anteroventrally, shape-selective neurons dorsally, and motion-selective neurons posteriorly. At the same time, partial overlap among these response classes was observed, with a subset of neurons exhibiting joint tuning across stimulus dimensions, suggesting an organizational scheme characterized by regional specialization and partial cross-feature integration. Notably, entopallium neurons exhibited a moderate level of visual feature integration and shared important functional properties with early to intermediate stages of mammalian visual processing. Together, these findings establish the entopallium as a major site for multidimensional visual analysis in birds and provide evidence for convergent principles underlying the evolution of complex visual systems across vertebrates.

Keywords: Entopallium; Tectofugal pathway; Feature encoding; Functional organization; Object recognition

INTRODUCTION

Avian vision has evolved along a neurobiological trajectory fundamentally distinct from that of mammals. Unlike the layered cortical architecture of mammals, the avian brain is organized into discrete nuclear structures with specialized visual functions (Karten, 2015). Two principal ascending visual pathways mediate visual information flow in birds, namely the tectofugal and thalamofugal pathways (Benowitz & Karten, 1976; Revzin & Karten, 1967). Among these, the tectofugal pathway represents the primary route for visual processing. Despite this markedly different neural architecture, birds exhibit sophisticated visual and cognitive capabilities, including object recognition (Pepperberg & Nakayama, 2016; Pusch et al., 2022; Soto & Wasserman, 2016), image categorization (Anderson et al., 2020a; Levenson et al., 2015; Navarro et al., 2020), rule learning (Qadri & Cook, 2017; Scarf et al., 2011), and visual memory (Anderson et al., 2020b; Johnston et al., 2017). While extensive anatomical and connectivity studies have mapped the components of the avian visual system in considerable detail, the neural basis underlying object perception and category-level representation remains poorly understood. A central unresolved issue, therefore, concerns how visual nuclei in the avian brain encode information relevant to object recognition.

The entopallium (ENTO), which receives the major tectofugal input, plays a central role in preserving and processing visual information in birds. Visual signals originating from the optic tectum (OT) are relayed via distinct subdivisions of the nucleus rotundus (RT) (Deng & Rogers, 1998; Hunt & Künzle, 1976; Nixdorf & Bischof, 1982), which project in a topographically organized manner to specific regions of the ENTO (Hellmann & Güntürkün, 2001; Krützfeldt & Wild, 2005). This anatomical arrangement preserves the spatial structure of projections and supports parallel processing streams along the tectofugal pathway. Additional specialization is evident within the ENTO itself. The entopallium core (Ec) contains large neurons that are relatively sparsely distributed, whereas the surrounding belt region (Eb) is composed of smaller and more densely packed neurons (Husband & Shimizu, 1999; Karten & Hodos, 1970; Krützfeldt & Wild, 2005). Projections extending from the Ec to Eb, and subsequently to higher associative areas, also retain

Received: 08 July 2025; Accepted: 02 September 2025; Online: 03 September 2025

Foundation items: This work was supported by the National Natural Science Foundation of China (62206253) and China Postdoctoral Science Foundation (2024M752934)

*Corresponding author, E-mail: wzz1982@zzu.edu.cn

a topographic organization along the anterior-posterior axis (Shanahan et al., 2013; Shimizu & Bowers, 1999). Although anatomical evidence suggests that functional channels remain segregated within the ENTO (Wang et al., 1993), direct electrophysiological confirmation of this organizational principle remains lacking.

Behavioral, lesion, and physiological studies have identified the ENTO as a critical node for visual feature processing in birds. Damage to this region impairs luminance discrimination, shape discrimination, and conspecific recognition in pigeons (Bessette & Hodos, 1989; Watanabe, 1991, 1994, 2003). These deficits also exhibit spatial specificity within the ENTO, with anterior lesions disrupting pattern recognition and posterior lesions impairing motion detection (Cook et al., 2013; Nguyen et al., 2004). At the neuronal level, ENTO neurons possess large receptive fields ranging from 20°–150°, with circular, elliptical, or irregular configurations (Engelage & Bischof, 1996; Gu et al., 2002; Xiao et al., 2006). Many neurons respond robustly to small moving stimuli and display selectivity for motion direction and speed, including a bias toward forward and downward movement trajectories (Gu et al., 2002; Kimberly et al., 1971). In the caudal ENTO, tau (τ) and eta (η) neurons form distinct populations that preferentially respond to looming and receding stimuli, respectively (Engelage & Bischof, 1996; Xiao et al., 2006), and each population exhibits distinct firing dynamics in response to approaching or receding stimuli. More recent work in awake pigeons has further linked the ENTO to object recognition and categorization (Azizi et al., 2019; Clark et al., 2022). However, converging evidence suggests that ENTO neurons may not directly support categorical representations. Consequently, despite important advances, a comprehensive functional characterization of ENTO neurons remains unavailable, particularly in comparison with the extensive body of knowledge on visual processing in the mammalian visual cortex.

In this study, receptive field properties and large-scale functional organization in the pigeon (*Columba livia*) ENTO were systematically examined. Visual stimulation paradigms adapted from primate vision research were combined with precise histological reconstructions to characterize neuronal responses to color, shape, and motion. Results revealed that ENTO neurons encoded visual features of intermediate complexity and were distributed in spatially distinct clusters according to feature selectivity. These findings provide direct electrophysiological support for a modular and topographically structured visual representation in the avian brain, shedding new light on the principles of mid-level visual processing beyond the mammalian cortex.

MATERIALS AND METHODS

Subjects

Recordings were obtained from 18 acutely prepared pigeons (*Columba livia*; males and females, approximately 1 year of age). Prior to experimentation, birds were housed individually under a natural light-dark cycle. A mixed grain diet was provided, and body weight was maintained at 80%–90% of free-feeding level, with water available *ad libitum*. All experimental procedures were reviewed and approved by the Life Sciences Ethics Review Committee of Zhengzhou University (No. ZZUIRB2022-44) and were conducted in accordance with the regulations of the Animal Care and Use Committee of Zhengzhou University.

Surgery

Animals were anesthetized with 20% urethane (1 mL/100 g body weight). Feathers surrounding the head and ear regions were removed, and each pigeon was secured in a custom stereotaxic apparatus (RWD Life Science Co., Ltd., China) aligned according to the topographic atlas of Karten and Hodos (Halpern et al., 1968). After stabilization, the scalp was incised to expose the skull. The recording target was localized stereotaxically, a craniotomy was performed with a microdrill, and the dura mater was then carefully incised. Neural activity was recorded using a 32-channel tungsten wire electrode (Ketou Brain-Machine Technology, China; 4×8 array, 350 μm spacing, 7 mm length, 800 kΩ impedance). The dorsoventral (DV) coordinate was defined as zero when the electrode contacted the brain surface, after which the electrode was advanced gradually to the target depth while minimizing tissue collapse. The ground wire was then embedded subcutaneously for reference. All recordings were obtained from the left ENTO, and the left eye was occluded to ensure visual stimulation was delivered exclusively to the right eye.

Neuronal recording

Neural signals were acquired, amplified, filtered, and digitized using the Cerebus multichannel data acquisition system (Blackrock Microsystems, USA) at a sampling rate of 30 kHz. To extract spiking activity, raw signals were band-pass filtered from 300 Hz to 5 kHz, and spike events were detected using a threshold of −4 to −6 times the standard deviations of baseline signal fluctuations. Key task events, including stimulus onset and offset, were synchronously recorded to enable subsequent analysis of task-related neural responses.

Spike sorting was performed with the Wave_clus 3 algorithm (Quiroga et al., 2004), and only neuronal activities showing statistically significant differences were retained for analysis. In most cases, analysis was based on a conservative multi-unit activity (MUA) strategy. Inter-spike interval (ISI) violation rates were also quantified for each recording site, and neurons with ISI violation rates <0.1% were classified as well-isolated units (Vincent & Economo, 2024) and analyzed separately (Supplementary Figure S1). Additionally, trough-to-peak duration (Oghazian et al., 2021) was used to broadly assign neurons to putative excitatory and inhibitory classes (Supplementary Figure S2). As no significant differences were detected in response properties between these two classes, this distinction was not carried forward in the main analyses.

Visual stimulus

A series of visual stimulation paradigms was used to characterize receptive field organization and neuronal responses to color, shape, and motion. All stimuli were generated in MATLAB (R2020a) with Psychophysics Toolbox (Psychtoolbox, PTB; version 3.0.17). Visual stimuli were presented on a 50 inch display with a 16:9 aspect ratio (AG485UD, AOC, China), positioned 20–40 cm from the head. Display parameters included a resolution of 3 840×2 160 pixels, refresh rate of 100 Hz, and DPI of 36.486 pixels/cm, corresponding to a maximum visual field coverage of 138°×112°. The screen was calibrated using a color calibration device before testing. In pigeons, the visual axis of the monocular field forms a 61° angle relative to the beak-tail axis. To align the display with the frontal visual field, the stereotaxic apparatus was rotated so that the screen was

positioned at a 29° angle. The natural angle between the beak-eye axis and horizontal plane is approximately 34°, whereas fixation in the stereotaxic apparatus shifted this angle to 72°. Therefore, the screen was rotated by 38° to match the normal visual field orientation (Supplementary Figure S3). Before each task, receptive fields were mapped and screen position was adjusted so that the receptive field center aligned with the display.

Receptive field mapping: Both static receptive fields (ON/OFF receptive fields) and motion receptive fields were mapped with sparse-noise stimuli and motion stimuli, respectively. For static receptive field mapping, the display field was uniformly divided into a 21×38 grid. A small square stimulus (3° in size) was flashed at random positions in four colors: red, yellow, blue, and green. Each presentation lasted for 500 ms and was followed by a 500 ms interval. For motion receptive field mapping, a square stimulus (3° in size) was moved at a speed of 117°/s along vertical and horizontal axes. Motion receptive fields were defined from the mean neuronal response across four directions of movement: up, down, left, and right. A neutral gray background was used throughout receptive field mapping.

Color stimulus: A total of 42 color stimuli were generated, comprising 36 chromatic stimuli and six grayscale stimuli (Figure 2A). Chromatic stimuli were defined in HSV color space using six hues (yellow, green, cyan, blue, purple, and red) and six luminance levels (Supplementary Table S1). After stimulus definition in HSV space, values were converted to RGB with the “hsv2rgb()” function in MATLAB. Saturation was fixed at 1, and only the value component was varied to generate luminance differences within each hue. All stimuli were presented within the mapped receptive field on a black background to minimize contrast-related effects (Supplementary Figure S4). Each color stimulus was delivered three times in randomized order. Stimulus duration was 500 ms, followed by a 30 s interstimulus interval to reduce neural adaptation (Supplementary Figure S5A–C), defined here as the gradual decrease in neuronal responsiveness during repeated or prolonged stimulation (Liu et al., 2013).

Before data collection, the monitor was gamma-corrected and color-calibrated with a standard calibration device (X-Rite i1Display Pro, X-Rite, Inc., USA) to ensure a linear relationship between RGB output and emitted light intensity, minimizing nonlinear distortion in luminance control. Luminance for all color stimuli was measured before presentation with a luminance meter (Konica Minolta LS-100, Konica Minolta, Inc., Japan), and all measured values are provided in the Appendix. MATLAB code used for stimulus generation and color conversion, along with the luminance measurement data, has been deposited in the project GitHub repository and Figshare dataset to facilitate reproduction on similarly calibrated systems.

Shape stimulus: Shape tuning was examined with a paradigm widely used in mammalian visual studies (Hegdé & Van Essen, 2007; Jiang et al., 2021; Pasupathy & Connor, 1999). A total of 120 stimuli was generated from combinations of angular structure, curvature, and orientation. Angular features included angles of 60°, 90°, 120°, and 150°. Curvature was categorized as either sharp or smooth. Orientation was sampled at 12 evenly spaced orientations spanning 0° to 360°. This stimulus set was designed to define shape selectivity in ENTO neurons. Each shape was presented in the preferred color of the recorded neuron, centered within the receptive field, and scaled to one-fourth of receptive field size. Stimulus duration was 500 ms, and the interstimulus interval was 30 s to minimize neural adaptation (Supplementary Figure S5A–C). Each stimulus was presented three times in a randomized order.

Looming and receding stimulus: Looming and receding stimuli were used to simulate objects approaching or moving away from the observer. On a gray background, a black object with an initial diameter of 50 cm at a starting distance of 10 m was simulated to approach or recede at a speed of 5 m/s (Dill, 1974). Each trial lasted 2.01 s, followed by an interstimulus interval of 30 s, and each condition was presented three times. For analysis, mean firing rate was calculated with a sliding window using a 50 ms bin and a 1 ms step. This analysis was used to determine whether neuronal response profiles were consistent with tau and eta neurons (Engelage & Bischof, 1996; Xiao et al., 2006).

Motion stimulus: Directional selectivity was assessed with motion stimuli presented in eight directions separated by 45° intervals over the full 0–360° range. Stimuli moved linearly at a speed of 62°/s within a circular area (72° in diameter) centered on the receptive field. Each motion trajectory crossed the receptive field center to maintain uniform speed and path length across directions. To examine modulation of motion responses by color and shape, six colors (red, blue, green, yellow, black, and white) and six shapes (90° bar, 0° bar, square, triangle, circle, and cross) were introduced, generating multiple stimulus conditions. Each condition was repeated three times, with a 1 s static presentation before motion onset to eliminate the influence of initial flashing. Because adaptation to motion stimuli was comparatively weak, the interstimulus interval was set to 12 s (Supplementary Figure S5D–F). Stimulus order was randomized.

Data analysis

Determination of reliable neural responses: Neuronal responses to each stimulus were quantified by subtracting baseline firing rate (−3 000 to 0 ms) from mean firing rate measured during the stimulus presentation window (50–500 ms). For each stimulus condition, the final response value was calculated as the mean across repeated trials (n=3). In receptive field mapping, ON and OFF responses were defined as mean firing rate within the 50–500 ms window following stimulus onset and offset, respectively. Firing rate curves were generated with a 100 ms sliding window advanced in 1 ms steps.

To identify neurons with reproducible stimulus-evoked activity, inter-trial correlation (ITC) of response profiles was evaluated using Pearson correlation coefficients (Garcia et al., 2018; Yoshida & Ohki, 2020). Thresholds for ITC were set at 0.3 for color stimuli, 0.25 for shape stimuli, and 0.4 for motion stimuli (Supplementary Figure S6). This approach effectively eliminated non-specific responses arising from extraneous factors in the experimental paradigm (e.g., flickering effects of visual stimuli). Such responses typically exhibited random and unpredictable firing patterns and therefore did not reflect genuine selectivity for visual stimulus features.

Receptive field mapping: Spatial response maps were constructed from neuronal response strength at each tested location. To reduce noise and enhance spatial continuity, maps were smoothed sequentially with a 3×3 median filter and a mean filter. Receptive field structure was then quantified by contour extraction followed by elliptical fitting, with the fitted

ellipse defined to match the second-order moments of the response region. Receptive field size was determined from the major and minor axes of the fitted ellipse.

To assess the spatial relationship between ON and OFF receptive fields, the Overlap Index (OI) was computed as:

$$OverlapIndex = \frac{Area(overlap)}{\min(Area(\text{on}), Area(off))} \quad (1)$$

where *Area(on)* represents the ON receptive field area, *Area(off)* represents the OFF receptive field area, and *Area(overlap)* denotes the overlapping area between the ON and OFF receptive fields.

Neuronal sensitivity to motion stimuli was quantified by summing the squared response intensities across all spatial locations within the receptive field:

$$E_{motion} = \sum_{x=1}^{N=48} \sum_{y=1}^{M=86} R(x,y)^2 \quad (2)$$

where $R(x,y)$ represents neuronal response magnitude at spatial location (x,y), and N and M correspond to the horizontal and vertical spatial dimensions of the receptive field, respectively.

Given that anesthetized pigeons do not exhibit active fixation and their exact gaze center cannot be determined, visual eccentricity was estimated relative to the mean receptive field center across all neurons recorded within each experiment. Two methods were used to estimate receptive field centers. In Method 1 (Supplementary Figure S7), each receptive field was fitted with an ellipse, and the center was measured relative to a reference point, defined as the mean receptive field center of all neurons recorded in the same experiment (spanning 2.45 mm along the AP axis). In Method 2 (Supplementary Figure S8), the receptive field center was defined as the location showing the maximum response within a 9×9 region, and eccentricity was calculated as the offset from the same reference point along the horizontal and vertical axes.

Quantification of neuronal tuning: To quantify neuronal tuning properties, three indices were defined: Selectivity Index (SI), Consistency Index (CI), and Sparsity Index (SPI). These indices were used to characterize neuronal selectivity for shape, color, and motion stimuli. For response data organized as $I \times J$ or $I \times J \times K$ matrices, such as hue×luminance, orientation×curvature×angle, or direction×color×shape, the data were restructured into an $M \times N$ matrix, where M represents the total number of stimulus conditions and N represents the dimension of a specific tuning curve, such as the number of hue levels or motion directions. Based on this transformation, SI, CI, and SPI were calculated as follows:

The SI quantified the strength of neuronal preference along a given stimulus dimension and was defined as:

$$SI = \frac{1}{M} \sum_{i=1}^{M} \frac{R_{preferred} - R_{null}}{R_{preferred} + R_{null}} \quad (3)$$

where $R_{preferred}$ denotes the neuronal response to the most effective stimulus within a given tuning curve, R_{null} denotes the neuronal response to the least effective stimulus within the same tuning curve, and M represents the number of stimulus conditions used in the analysis. SI values range from 0 to 1, with higher values indicating stronger selectivity for a specific stimulus dimension.

The CI quantified the extent to which a neuron preserved its tuning preference despite variations in stimulus dimensions, and was calculated from pairwise Spearman correlation coefficients:

$$CI = \frac{2}{M(M-1)} \sum_{i=1}^{M-1} \sum_{j=i+1}^{M} p(R_i, R_j) \quad (4)$$

where $p(Ri,Rj)$ represents the Spearman correlation coefficient between neuronal responses under *i-th* and *j-th* stimulus conditions and M represents the total number of stimulus conditions. Negative $p(Ri,Rj)$ values were set to 0 to exclude cases where responses exhibit an inverse relationship. CI values range from 0 to 1, with values closer to 1 indicating higher tuning consistency.

The SPI quantified the degree to which a neuron responded selectively to a restricted subset of stimuli within the entire stimulus set (Zoccolan et al., 2007) and was defined as:

$$SPI = \left(1 - \frac{\left(\sum_{i=1}^{t} R_i/t\right)^2}{\sum_{i=1}^{t}(R_i^2/t)}\right) / \left(1 - \frac{1}{t}\right) \quad (5)$$

where R_i represents the neuronal response to the *i-th* stimulus and $t = M \times N$ denotes the total number of stimuli in the set. SPI values range from 0 to 1, with SPI=0 indicating no selectivity (neuron responds equally to all stimuli) and SPI=1 indicating maximum selectivity (neuron responds exclusively to a single stimulus).

Dimensionality reduction analysis: To characterize stimulus-specific response patterns across neuronal clusters, multidimensional scaling (MDS) was applied to reduce the dimensionality of population response data and visualize the resulting distributions. An $M \times N$ response matrix R was first constructed, where M represents the number of stimuli and N represents the number of neurons. Matrix R was then normalized to eliminate differences in response magnitudes across neurons. The MDS algorithm was subsequently used to project the high-dimensional response matrix into a two-dimensional space, yielding a transformed $M \times 2$ matrix. Finally, a 2D scatter plot was used to visualize the distribution of neuronal responses in the low-dimensional space.

Clustering analysis of looming and fading response patterns: To analyze neuronal firing patterns evoked by looming and fading stimuli, a clustering analysis was conducted. For each neuron, mean firing rate was calculated with a 100 ms time window (bin) advanced in 10 ms steps over an interval spanning 200 ms before stimulus onset to 200 ms after stimulus offset, corresponding to a total duration of 2 410 ms. This procedure generated a 217×241 response matrix, where 217 represents the number of neurons and 241 represents the time dimension. K-means clustering was then applied to classify response patterns, with responses to looming and fading stimuli analyzed separately and partitioned into four categories. To illustrate temporal response dynamics within each cluster, mean±standard deviation (SD) response curves were plotted.

Decoding analysis: To assess the information carried by neuronal populations, decoding analyses were performed for classification of 42 color stimuli and 288 motion stimuli. Training labels were first assigned based on stimulus category (e.g., color, hue, motion direction, or shape). Decoding performance was assessed by five-fold cross-validation. To determine the effect of population size, a specified number of

neurons was randomly sampled from the entire population 50 times.

For decoding based on mean firing rate without explicit temporal information, a Linear Support Vector Machine (SVM) classifier was used. This decoder provides a simple and biologically plausible linear framework and has been shown to effectively link inferior temporal (IT) neuronal activity with primate behavior (Majaj et al., 2015). Responses from individual neurons were treated as input features, and the SVM optimized linear decision boundaries to maximize classification performance.

For decoding incorporating temporal dynamics, a long short-term memory (LSTM) network was employed. The network architecture consisted of an initial layer with 64 neurons, an intermediate layer with 32 neurons, and an output layer. Input data consisted of firing-rate time series calculated in 100 ms time windows with a 100 ms step following stimulus onset, yielding 14 time points per trial. This model was used to determine whether temporal response sequences carried significant decoding information and to assess the contribution of response dynamics to decoding accuracy.

Statistical analysis: All statistical analyses were conducted in Python. Pearson correlation coefficients (r) were used to assess linear correlations in normally distributed data, whereas Spearman correlation coefficients (ρ) was applied for non-normal distributions or non-linear relationships. Paired t-tests were used to compare means within the same neuron, with Bonferroni correction for multiple comparisons. The Mann-Whitney U-test was employed for non-normally distributed data. Repeated-measures analysis of variance (ANOVA) was used to compare mean differences across multiple conditions. Statistical significance was defined as P=0.05. Data are reported as mean±SD. For non-normally distributed data, non-parametric tests were prioritized to ensure robust statistical inference.

Histological analysis

Electrode implantation targeted the ENTO region using the following stereotaxic coordinates: anteroposterior (AP): 8.25–11.25 mm, mediolateral (ML): 5.0–6.0 mm, and dorsoventral (DV): 4.0–5.0 mm. A total of 18 penetrations were performed within this range. Given the 350 μm spacing of the 4×8 electrode array, penetration sites were selected to maximize spatial coverage of the ENTO. Each penetration was maintained at a fixed location during data collection, and the recording site was marked at the end of the session by electrolytic lesioning (0.3 mA for 30 s). Within the 4×8 array, electrolytic lesions were delivered through two reference channels, namely the rostral-medial and caudal-lateral channels (Supplementary Table S2), so that positions of the remaining electrodes could be inferred relative to these fixed landmarks.

At the end of the experiment, animals were euthanized with an overdose of 20% urethane and transcardially perfused. Perfusion involved an initial rinse with phosphate-buffered saline (PBS, Biosharp, China), followed by fixation with 4% paraformaldehyde (PFA, Servicebio, China). Brains were removed and post-fixed in 4% PFA for 12 h, then cryoprotected in 30% sucrose solution at 4°C for 48 h. Tissue was then frozen and sectioned coronally at a thickness of 20 μm with a cryostat. All sections were subjected to Nissl staining and examined microscopically to verify electrode tracks and lesion sites (Supplementary Figure S3C). Across all penetrations, sampling was designed to maximize coverage of the ENTO region (Supplementary Figure S3D). Each penetration site was mapped to a standard brain atlas, enabling the determination of standardized site coordinates. Detailed histological verification for all penetration sites is provided in Supplementary Figure S9.

RESULTS

Activity was recorded from 558 neurons in the pigeon ENTO across 18 electrophysiological sessions, including both single-unit and multi-unit signals, and receptive field organization together with feature selectivity was systematically examined. During recording, visual stimuli varying in color, shape, and motion were presented to define response properties across multiple stimulus dimensions. Electrode positions were verified histologically to reconstruct the spatial distribution of functional properties. For each task, recording sites exhibiting responses that exceeded baseline activity by more than 20% were classified as “responsive”, whereas sites with ITC values above predefined thresholds were labeled as “high-reliability sites” (Garcia et al., 2018; Yoshida & Ohki, 2020). ITC thresholds were set at 0.3 for color, 0.25 for shape, and 0.4 for motion (Supplementary Figure S6). Sites with ISI violation rates below 0.1% were classified as well-isolated units and analyzed separately (Supplementary Figure S1). For consistency, all recorded units are referred to as “neurons” throughout the manuscript.

Topographic variations in ENTO receptive fields

Well-defined receptive field structure was observed in most ENTO neurons (498/558, 89.2%). Among these neurons, 390 (78.3%) responded to both ON/OFF and motion stimuli, while 108 (21.7%) responded exclusively to ON/OFF stimuli. Within the ON/OFF-responsive population, 352 neurons (70.7%) exhibited both ON and OFF responses, whereas 146 neurons (29.3%) showed only ON responses. Three-dimensional spatial mapping of receptive field types (Supplementary Figure S10A, right panel) revealed substantial overlap between neurons lacking OFF responses and neurons unresponsive to motion stimuli (84/142, 58.7%). These neurons were predominantly localized to anterior and ventrolateral regions of the ENTO, suggesting the existence of functionally distinct neuronal subtypes within these areas.

Both ON and OFF receptive fields displayed circular, elliptical, or irregular configurations, with some neurons exhibiting one or two localized response peaks (Figure 1A, exp6_ch15, exp3_ch24), consistent with previous observations (Gu et al., 2002; Xiao et al., 2006). In contrast, motion-responsive fields were typically more irregular and either remained confined to the upper visual field (Figure 1A, exp1_ch6, exp6_ch15) or extended across nearly the full visual field (Figure 1A, exp14_ch13). To quantify receptive field shapes, ellipses were fitted to the ON and OFF receptive fields. ON receptive fields showed a major axis of 128.2±4.6° (mean±SD) and a minor axis of 102.7±5.6° (Figure 1B), whereas OFF receptive fields showed a major axis of 121.7±8.3° (mean±SD) and a minor axis of 91.5±9.1° (Figure 1C). In both cases, the major axis exceeded the minor axis significantly (two-sided paired t-test, P<0.001), indicating a consistent elongated profile. Based on equivalent circular diameter, ON fields were larger than OFF fields (101.6±2.0° vs. 93.3±4.5°; two-sided paired t-test, P<0.001), consistent with stronger sensitivity to stimulus onset (Figure 1D).

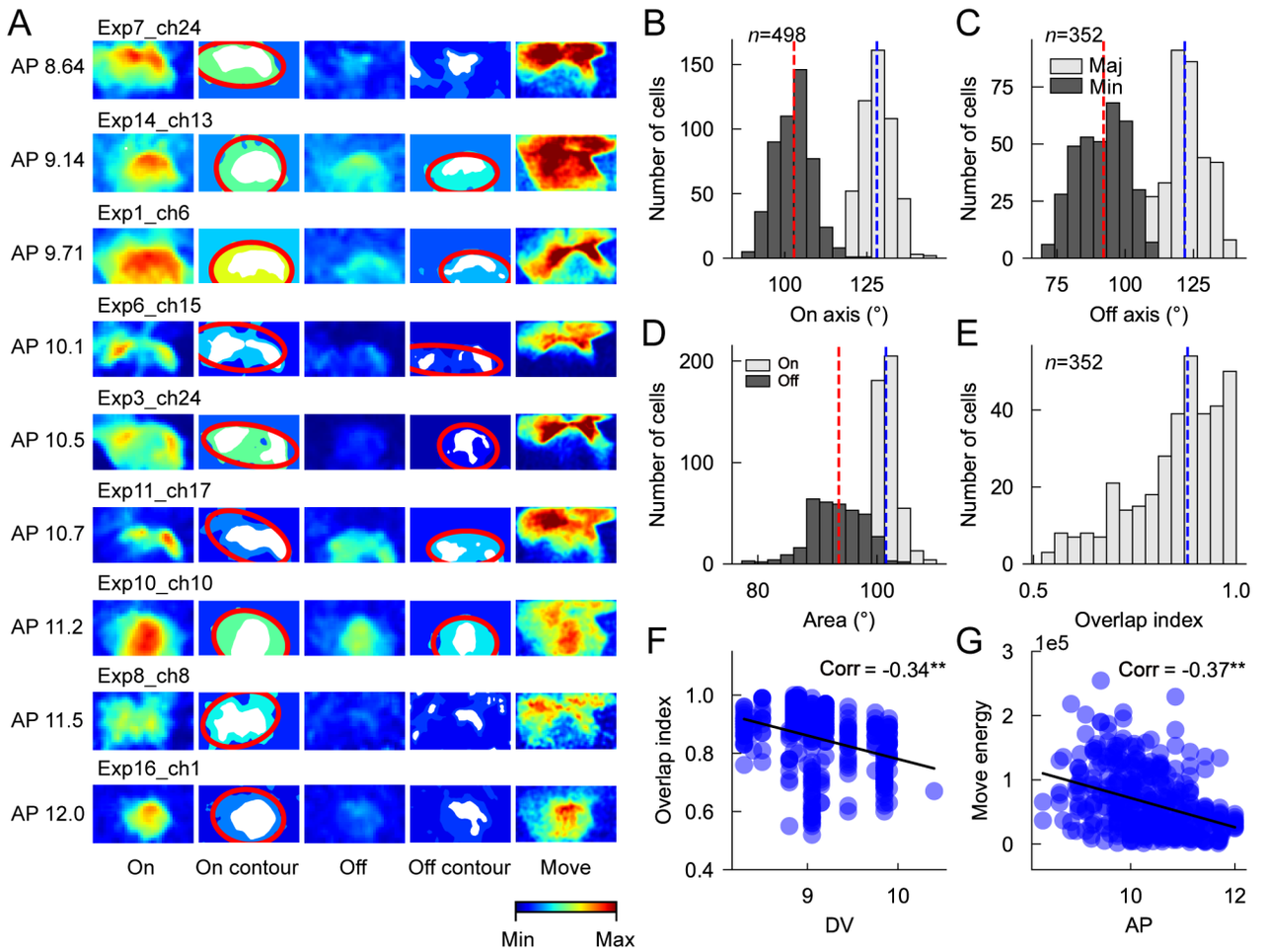

Figure 1 Receptive field structure of ENTO neurons

A: Representative receptive field profiles of selected neurons distributed along the AP axis. From left to right: On receptive field, On receptive field contour, Off receptive field, Off receptive field contour, and motion receptive field. Red ellipses indicate fitted results. B: Distribution of major and minor axes for On receptive fields. Light gray bars represent major-axis length, and dark gray bars represent minor-axis length. Major axes were significantly longer than minor axes (two-sided paired *t*-test, $P<0.001$, $n=498$). C: Distribution of major and minor axes for Off receptive fields. Major axes were significantly longer than minor axes (two-sided paired *t*-test, $P<0.001$, $n=352$). D: Distribution of equivalent diameters for On and Off receptive fields. Equivalent diameter was significantly greater for On than for Off receptive fields (two-sided paired *t*-test, $P<0.001$, $n=352$). E: Distribution of overlap indices between On and Off receptive fields. Median overlap index was 0.88, and minimum value was 0.52. F: Overlap index showed a significant negative correlation with neuronal depth (Pearson correlation coefficient $r=-0.34^{***}$, $n=352$). G: Motion response energy showed a significant negative correlation with anteroposterior position (Pearson correlation coefficient $r=-0.37^{***}$, $n=390$).

Furthermore, ON and OFF subregions from the same neurons exhibited substantial spatial overlap (overlap index=0.85±0.11), supporting integrated encoding of luminance increments and decrements within individual ENTO neurons (Figure 1E). Unlike cats and monkeys, in which visual eccentricity can be standardized relative to the fovea or area centralis (Orban et al., 1986), anesthetized pigeons do not maintain a fixed point of gaze. Therefore, receptive field eccentricity was estimated relative to a reference point defined as the mean center of all neuronal receptive fields recorded within each experiment. Under this relative framework, no systematic relationship was detected between eccentricity and anatomical location (Supplementary Figure S7, S8). Together, these results suggest that ENTO neurons generally possess large receptive fields and low eccentricity.

Receptive field organization also varied systematically with anatomical position in the ENTO. Along the AP axis, central neurons tended to exhibit bilobed fields, anterior neurons showed smaller fields, and posterior neurons displayed stronger motion sensitivity. Quantitative analysis confirmed significant correlations between receptive field parameters and recording location (Supplementary Figure S11). Specifically, ON field size was negatively correlated with AP position (Pearson correlation coefficient $r=-0.22^{***}$), positively correlated with ML position (Pearson correlation coefficient $r=0.2^{***}$), and negatively correlated with DV position (Pearson correlation coefficient $r=-0.22^{***}$). These findings indicate that neurons in the dorsomedial anterior region had smaller receptive fields, whereas neurons in the ventrolateral posterior region had larger receptive fields. Moreover, overlap indices were negatively correlated with DV position (Figure 1F, Pearson correlation coefficient $r=-0.34^{***}$), and motion response energy increased toward the posterior ENTO (Figure 1G, Pearson correlation coefficient $r=-0.37^{***}$). Although heterogeneity in receptive field structure does not by itself establish discrete neuronal types, these spatial gradients support the presence of functionally diverse neuronal subpopulations within the ENTO.

Hue-dominant color representation in the ENTO

Color tuning in ENTO neurons was examined with 42 color stimuli defined by seven hues and six luminance levels (Figure 2A). Recordings were obtained from 498 color-responsive neurons, including 148 high-reliability units. Neuronal responses typically emerged approximately 50 ms after stimulus onset (Figure 2A, raster plot) and exhibited marked diversity in temporal profile, as revealed by firing-rate analyses based on 100 ms bins with a 1 ms sliding step. Five major response patterns were identified from these temporal

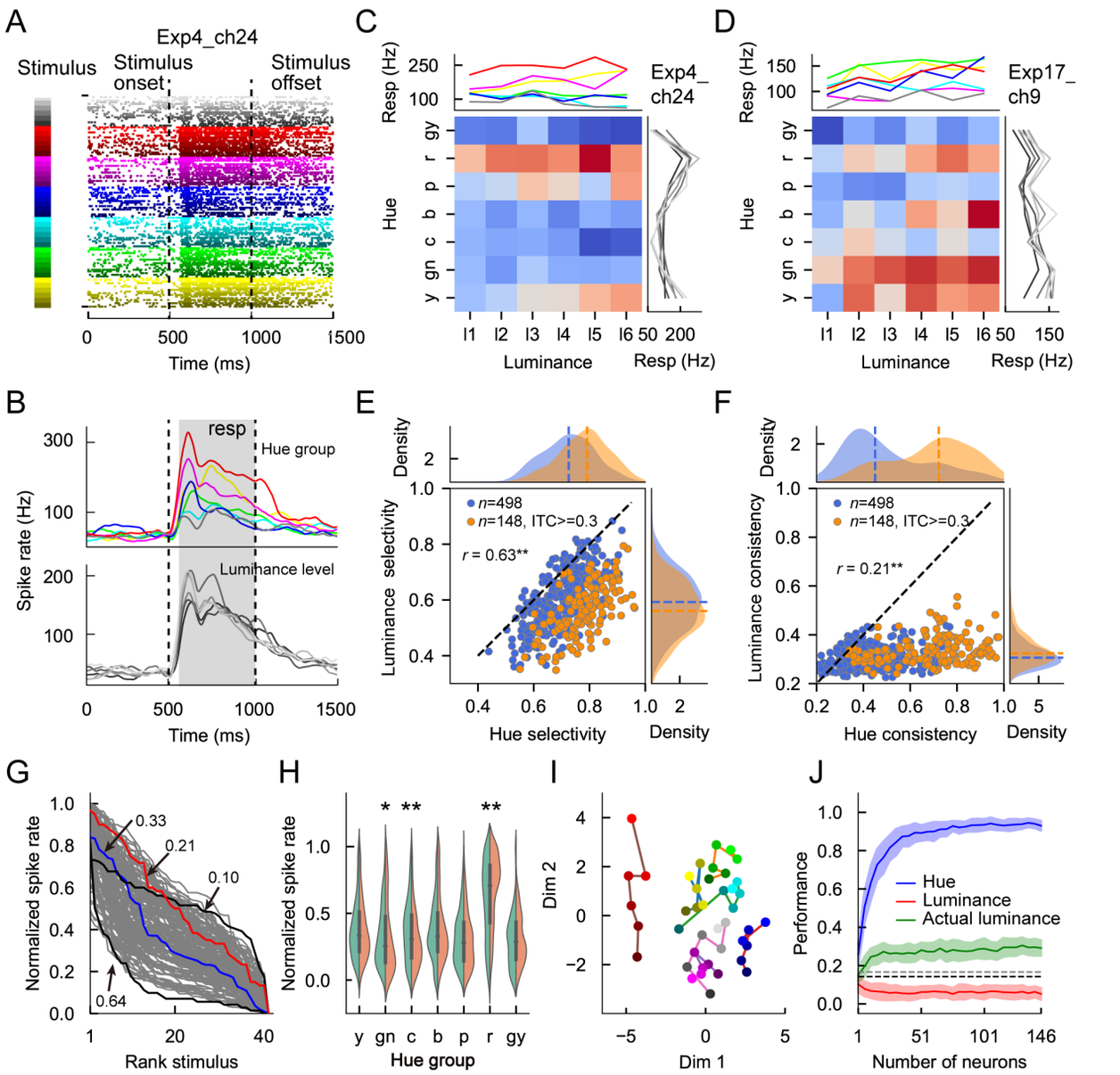

Figure 2 Color response properties of ENTO neurons

A: Color stimuli and raster responses from representative neurons. Left panel: 42 color stimuli (7 hues × 6 luminance). Right panel: Raster plots from representative neurons. Dashed lines indicate stimulus onset and offset. B: Mean firing-rate curves corresponding to raster plot in Figure 2A. Responses are grouped by hue and luminance. C: Representative neuron with high hue consistency. Heatmap: Mean firing-rate responses across all stimuli, with red indicating high responses and blue indicating low responses. Columns indicate luminance levels (l1–l6, from lowest to highest value component in HSV space), and rows indicate hue (y: Yellow; gn: Green; c: Cyan; b: Blue; p: Purple; r: Red; gy: Grayscale). Top panel: Luminance tuning curves, with each curve corresponding to one hue group. Right panel: Hue tuning, with each curve corresponding to one luminance group. D: Representative neuron with high luminance consistency. E: Comparison of luminance and hue selectivity. Blue dots represent all 498 responsive neurons, and orange dots represent 148 high-reliability neurons. Top panel: Probability distribution of hue selectivity. Right panel: Probability distribution of luminance selectivity. F: Comparison of luminance and hue consistency. G: Rank-ordered response curves used to quantify sparsity. Blue line represents neuron from Figure 2C, red line represents neuron from Figure 2D, and black lines indicate neurons with maximum and minimum sparsity values (Supplementary Figure S14). H: Population-level preference statistics. Low-luminance group: L1–L3 (green portion in violin plot); High-luminance group: L4–L6 (red portion in violin plot). Asterisks in the plot indicate hues showing significant response differences between luminance subgroups, assessed using two-sided *t*-test (*: $P<0.05$; **: $P<0.01$). I: Distribution of stimuli in MDS-reduced space. J: Decoding performance of neuronal populations. Black dashed line indicates chance level for hue decoding, and gray dashed line represents chance level for luminance decoding. Shaded areas denote standard deviation of decoding accuracy across 50 random subsampling iterations.

patterns, including sustained decay (Figure 2B), transient, sustained, highly selective, and ON-OFF responses (Supplementary Figure S12). This temporal heterogeneity suggested the presence of distinct neuronal subtypes or alternative temporal coding strategies for color representation. For further analysis, tuning strength was quantified as the mean firing rate during the 50–500 ms stimulus presentation window (Figure 2B).

ENTO neurons showed a pronounced tendency to preserve hue preference across changes in luminance. Tuning-curve analysis demonstrated that some neurons were strongly biased toward particular hues and retained this preference across luminance conditions (Figure 2C, red-preferring neuron). In contrast, other neurons demonstrated clear luminance sensitivity, exhibiting a consistent preference for higher luminance levels in luminance-tuning curves (Figure 2D, top panel) together with luminance-dependent changes in hue tuning (Figure 2D, right panel). To quantify these response characteristics, selectivity and consistency indices were calculated for both hue and luminance. Across the population, neurons exhibited significantly higher hue selectivity (0.72±0.09) compared to luminance selectivity (0.59±0.10; two-sided paired *t*-test, $P<0.001$, $n=148$). Notably, hue and luminance selectivity were strongly positively correlated (Figure 2E; Pearson correlation coefficient $r=0.63$), indicating that these stimulus dimensions were not independently encoded but were jointly processed within an integrated response framework in the ENTO. Analysis of tuning consistency further showed that hue consistency (0.50±0.18) significantly exceeded luminance consistency (Figure 2F; 0.32±0.05; two-sided paired *t*-test, $P<0.001$, $n=148$). These effects were even more pronounced among high-reliability neurons (ITC>0.3), supporting the conclusion that ENTO neurons primarily support luminance-invariant color representation.

To define population-level organization of color coding, tuning properties from 148 high-reliability ENTO neurons were analyzed collectively. Neuronal sparsity showed a median value of 0.28 across the population (Figure 2G), with representative neurons from Figure 2C and 2D exhibiting sparsity values of 0.31 and 0.21, respectively. Spatial analysis further indicated that color sparsity was not uniformly distributed across the ENTO, as neurons in the anteroventral region displayed significantly greater color selectivity than neurons in other regions (Supplementary Figure S10B). When single-neuron tuning profiles were integrated at the population level, responses showed a strong bias toward red hues (Figure 2H; paired two-sided Wilcoxon test with Bonferroni correction, $P<0.001$), resembling color biases described in primate visual systems (Liu et al., 2020). Within hue-specific luminance analyses, neuronal responses differed significantly across luminance levels for several hues, including green (two-sample *t*-test, $P=0.04$), cyan ($P<0.001$), and red ($P<0.001$).

To resolve the representational structure underlying these response biases, MDS was applied to population activity patterns. In the resulting low-dimensional space, stimulus representations clustered primarily according to hue, with red and blue exhibiting the greatest separation from other colors (Figure 2I), consistent with the hue biases identified in tuning analyses. Along the second component axis, stimuli were further separated according to luminance, with luminance-related separations again most prominent for red and blue hues. Decoding analysis provided quantitative support for these observations. In hue classification, a population of only 56 neurons yielded an accuracy of 91.6%±3.6% (Figure 2J). In contrast, decoding based on perceived luminance failed to exceed chance performance, while classification based on physical luminance achieved 29.6%±4.6% accuracy, significantly exceeding the chance level of 16.7%. Together, these results indicate that color coding in the ENTO is driven predominantly by hue, whereas luminance information is represented more weakly and in a hue-dependent manner, with the strongest contribution observed for red and blue stimuli.

Shape selectivity and invariance in the ENTO

Shape coding in the ENTO was examined using a set of 120 parametrically defined stimuli, excluding bar stimuli, that systematically varied along three feature dimensions: orientation, angle, and curvature. Responses were recorded from 475 ENTO neurons that showed significant activation to shape stimuli, including 148 high-reliability units (ITC>0.25). Shape selectivity was first assessed with a sparsity index, where 0 indicates uniform responses and 1 indicates exclusive responses to a single stimulus. Some neurons displayed broad tuning profiles (Figure 3A, sparsity=0.05), responding to most shapes while showing reduced activity for stimuli oriented around 90°–120°. Other neurons exhibited marked selectivity for specific configurations (Figure 3B, sparsity=0.16). Across the population of high-reliability neurons, median sparsity reached 0.13 (Figure 3C), indicating that a substantial fraction of ENTO neurons display pronounced shape selectivity.

Analysis of feature tuning revealed that orientation exerted the strongest influence on ENTO neuronal responses. The orientation selectivity index (OSI) was highest across the three measured dimensions (0.68±0.09, Figure 3D), significantly exceeding both angle selectivity (ASI: 0.36±0.05, two-sided paired *t*-test, Bonferroni-corrected $P<0.001$) and curvature selectivity (CSI: 0.19±0.03, $P<0.001$) across the population ($n=120$). Angle selectivity also significantly exceeded curvature selectivity ($P<0.001$). This hierarchy was consistent with the structure of the stimulus set, in which orientation differences constituted the most prominent variation at the pixel level. Notably, OSI, ASI, and CSI were positively correlated (Supplementary Figure S13, Pearson correlation coefficient $r=0.83$, 0.67, and 0.76, respectively), suggesting that neurons with strong selectivity along one dimension tended to show elevated selectivity along the others.

A subset of neurons also exhibited significant modulation by angle and curvature. For example, the neuron shown in Figure 3A displayed significant differences among angle groups (repeated measures ANOVA, $F=3.03$, $P=0.04$). The neuron shown in Figure 3B responded less strongly to the 60° angle group than to the 90° group (paired *t*-test with Bonferroni correction, $P<0.01$, middle-bottom of Figure 3B) and responded more strongly to smooth stimuli than to sharp stimuli (two-sided paired *t*-test, $P=0.01$, bottom-right of Figure 3B). However, neurons with significant modulation along these dimensions constituted a minority of the population (Figure 3F), with 20.5% (26/127) showing angle-related modulation and 16.5% (21/127) showing curvature-related modulation. These findings provide evidence that ENTO neurons encode multiple shape dimensions.

Beyond selectivity, ENTO neurons also showed partial

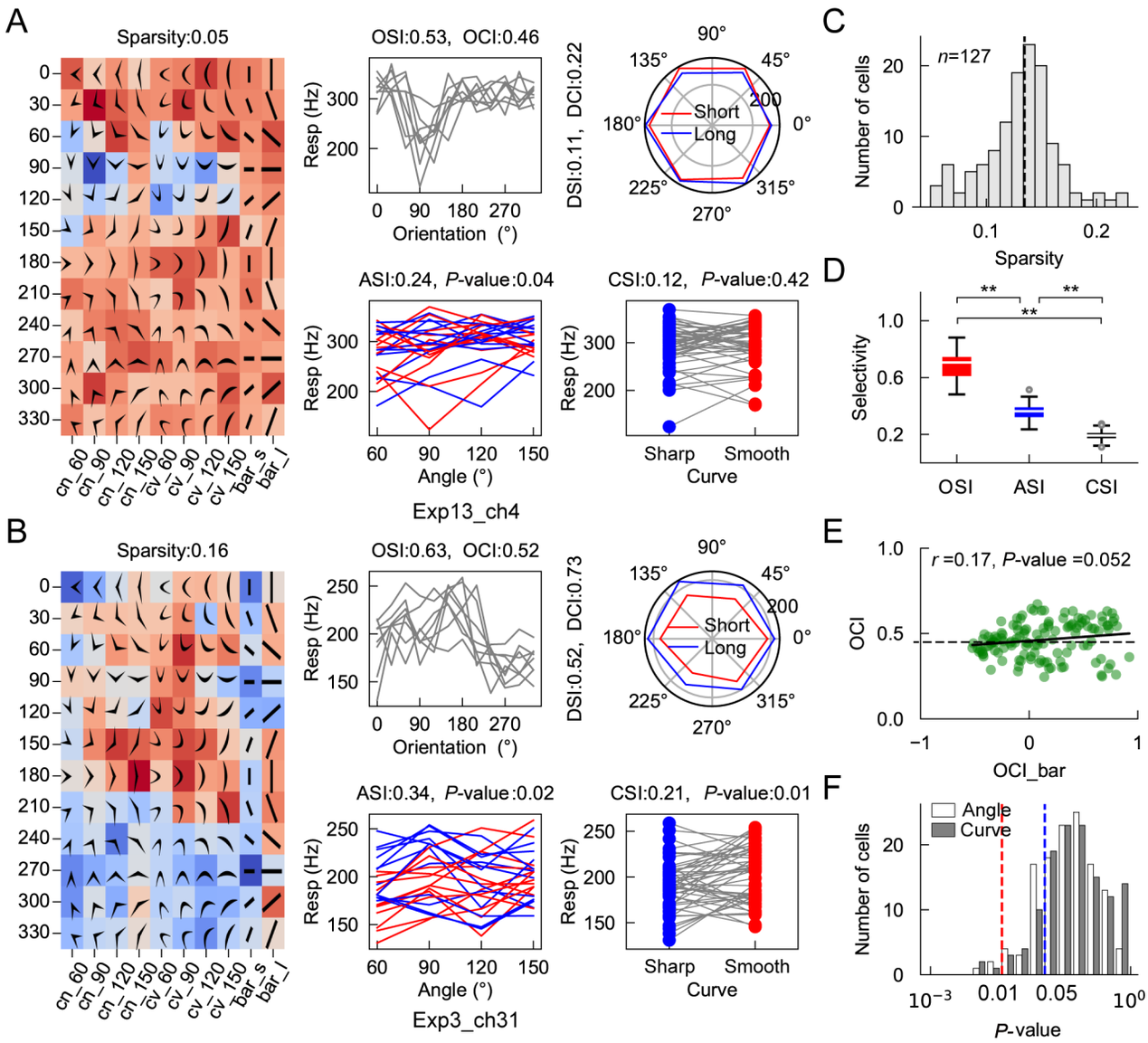

Figure 3 Shape response properties of ENTO neurons

A: Representative neuron with low sparsity. Left panel: Heatmap of responses to 120 stimuli varying in orientation, angle, curvature, and two bar lengths. Red indicates high responses, and blue represents low responses. Top middle panel: Orientation tuning curves, with each gray line representing responses to a specific shape (10 types). Bottom middle panel: Angle tuning curves (four angles); red indicates the sharp group, blue indicates the smooth group. "*P*" indicates repeated-measures ANOVA results for angle groups. Top right panel: Radar plot of bar stimulus responses; red represents short-bar stimuli, blue represents long-bar stimuli. Bottom right panel: Comparison between curvature groups (sharp vs. smooth). "*P*" indicates two-sided paired *t*-test results between curvature groups. B: Representative neuron with high sparsity. C: Distribution of sparsity values across the neuronal population. Black dashed line indicates median sparsity value (0.13). D: Comparison of orientation, angle, and curvature selectivity. Two-sided paired *t*-test with Bonferroni correction: *: $P<0.05$; **: $P<0.01$. E: Scatter plot of orientation consistency for bar and angle stimuli. Black dashed line represents median orientation consistency for angle stimuli (0.46). F: Distribution of repeated-measures ANOVA results for angle and curvature groups. Red dashed line indicates $P=0.01$, and blue dashed line indicates $P=0.05$.

invariance in orientation tuning. To quantify the stability of orientation preference across different stimuli, an orientation consistency index (OCI) was calculated, with a value of 1 indicating perfect stability. Representative neurons shown in Figure 3A, B (top-middle panels) demonstrated highly consistent orientation preferences across varying stimulus dimensions, with OCI values of 0.46 and 0.52, respectively. At the population level, mean OCI reached 0.46±0.10 (Figure 3E), indicating that ENTO neurons preserved a moderate degree of orientation tuning despite variation in other stimulus features. To further assess the generality of this tuning, responses to long-bar and short-bar stimuli were compared. Some neurons preserved consistent orientation preferences across stimulus classes (Figure 3B, top-right panel, OCI=0.73), whereas others showed reversed tuning (OCI<0), suggesting an interaction between orientation and stimulus length. Notably, OCI values derived from bar stimuli were not significantly correlated with OCI values derived from angle stimuli (Pearson correlation coefficient $r=0.17$, $P=0.052$; Figure 3E), indicating that orientation information alone does not fully explain shape tuning in the ENTO. Collectively, these findings suggest that ENTO neurons encode shape features through complex, multidimensional integration, combining selective feature tuning with partial invariance across stimulus

transformations.

Robust direction selectivity and feature integration in ENTO motion processing

Motion processing in the ENTO was examined using stimuli presented in eight directions and systematically varied in color and shape. Responses were recorded from 493 ENTO neurons that showed significant activation to motion stimuli, including 304 high-reliability units (ITC>0.4). These neurons exhibited robust directional tuning while concurrently incorporating additional visual attributes, particularly color and shape. ENTO neurons demonstrated pronounced selectivity for motion direction (Figure 4A, left panel), and preferred directions remained largely stable despite variations in stimulus color or shape, as reflected by highly consistent direction tuning curves under all stimulus conditions

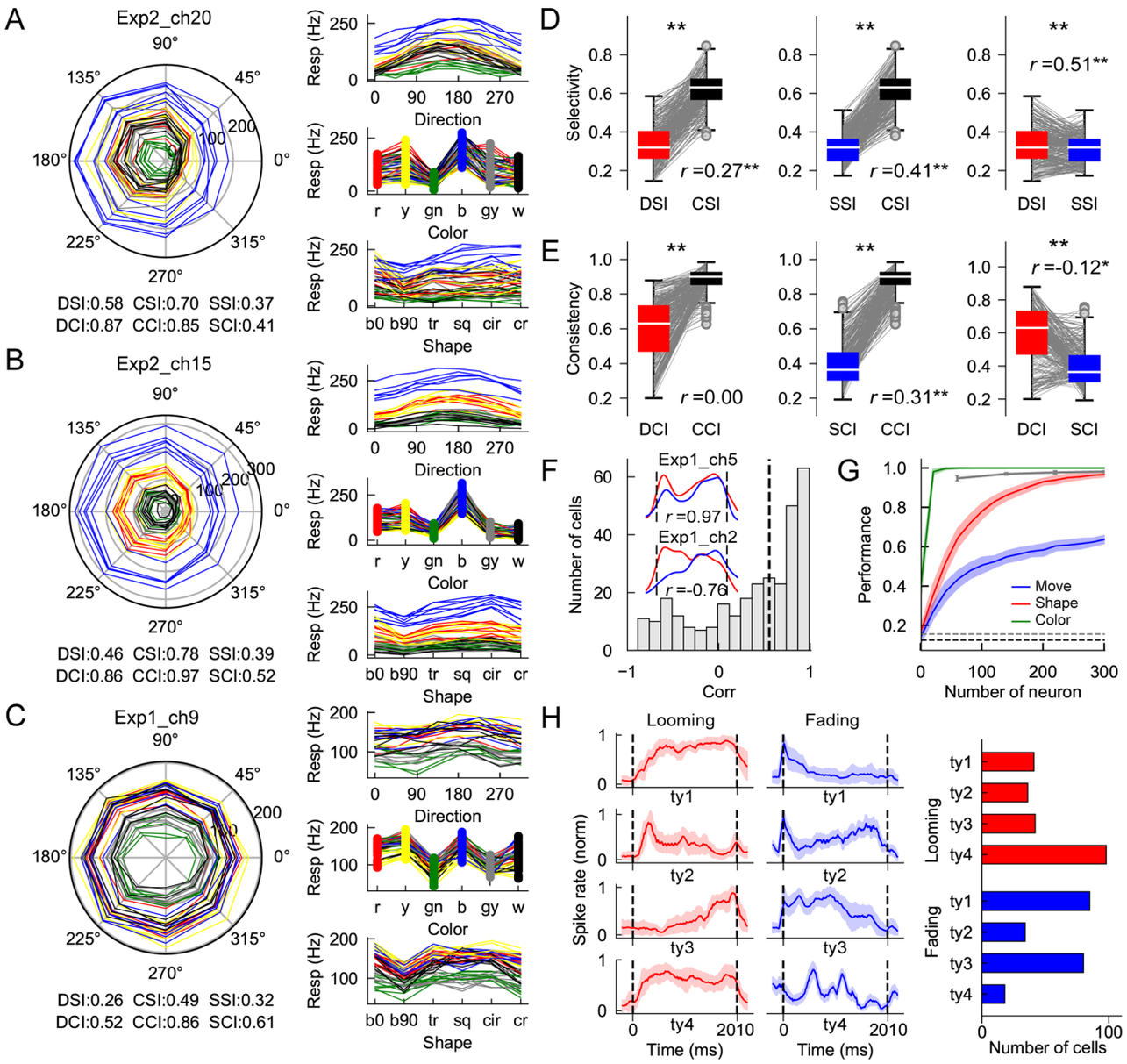

Figure 4 Motion response properties of ENTO neurons

A: Representative neuron with high motion direction consistency. Motion stimuli varied across eight directions, six colors, and six shapes. Left panel: Polar plot of neuronal responses to motion direction, smoothed using mean response of adjacent directions. Selectivity and consistency indices for direction, color, and shape are shown below. Top right panel: Direction tuning curves, with line color indicating stimulus color. Middle right panel: Color tuning curve, with line color indicating stimulus shape. Bottom right panel: Shape tuning curve, with line color indicating stimulus color. B: Representative neuron with high color consistency. C: Representative neuron with high shape consistency. D: Comparison of neuronal selectivity across motion stimulus dimensions. Statistical comparisons were performed using two-sided paired *t*-test with Bonferroni correction, *: $P<0.05$; **: $P<0.01$. E: Comparison of neuronal consistency across motion stimulus dimensions. F: Path-dependent and time-dependent neurons. Classification was based on the correlation between firing trajectories evoked by preferred and opposite motion directions. G: Decoding accuracy of motion attributes from neuronal populations. Shaded areas represent standard deviation of decoding accuracy across 50 random subsampling iterations. Gray line represents LSTM-based decoding of motion direction, repeated 30 times. H: Response patterns to looming and fading stimuli. Left panel: K-means clustering grouped looming- and fading-response patterns into four categories based on 217 reliably responsive neurons. Right panel: Distribution of neurons across identified response categories.

(Figure 4A, top-right panel). At the same time, many motion-sensitive neurons also exhibited selectivity for stimulus color and shape. For example, the neuron shown in Figure 4B preferred motion near 180° but responded significantly more strongly to blue stimuli than to other colors (Figure 4B, middle-right panel). Similarly, the neuron shown in Figure 4C preserved a stable preferred motion direction while exhibiting clear shape selectivity; although no clear color grouping was observed in the color tuning curve (where line colors correspond to shape attributes), the shape tuning curve showed significantly lower responses to the 90° bar stimulus relative to other groups (paired *t*-test with Bonferroni correction, $P<0.001$, $n=48$). Together, these findings suggest that ENTO neurons retain robust directional tuning during motion processing while integrating additional stimulus features such as color and shape.

Selectivity and consistency for direction, color, and shape were quantified across ENTO neurons during motion stimulation. Among the 304 high-reliability neurons, color selectivity (0.62±0.09) exceeded both direction selectivity (0.33±0.10; two-sided paired *t*-test with Bonferroni correction, $P<0.001$) and shape selectivity (0.31±0.07; Bonferroni-corrected $P<0.001$), while direction selectivity exceeded shape selectivity (Bonferroni-corrected $P<0.001$, Figure 4D). These results indicate that ENTO neurons retain a strong capacity for color discrimination even in the context of dynamic motion. Analysis of response consistency produced a similar pattern. Color consistency (0.88±0.07) was significantly higher than both shape consistency (0.40±0.12, two-sided paired *t*-test with Bonferroni correction, $P<0.001$) and direction consistency (0.59±0.18, Bonferroni-corrected $P<0.001$), while direction consistency exceeded shape consistency (Bonferroni-corrected $P<0.001$, Figure 4E). Notably, direction consistency showed little or no association with color consistency (Pearson correlation coefficient $r=0.00$) or shape consistency (Pearson correlation coefficient $r=-0.12^{*}$, $P<0.05$), suggesting limited functional overlap between directional coding and these additional stimulus dimensions. In contrast, color consistency and shape consistency were positively correlated (Pearson correlation coefficient $r=0.31^{**}$, $P<0.01$), indicating coordinated integration of these two features during motion processing in the ENTO.

Motion responses in individual ENTO neurons also exhibited distinct temporal dynamics. Analysis of firing-rate trajectories for preferred and opposite motion directions (Figure 4F, red and blue lines) identified two principal response types, namely path-dependent and time-dependent patterns. Path-dependent neurons showed strong correlation between firing trajectories evoked by opposite directions of motion (e.g., Figure 4F, exp1_ch5; Pearson correlation coefficient $r=0.97$), indicating that activity primarily reflects spatial position along the motion path. In contrast, time-dependent neurons exhibited weak or negative correlations (e.g., Figure 4F, exp1_ch2, Pearson correlation coefficient $r=-0.76$), suggesting that their firing patterns are driven more by motion timing than spatial trajectory. At the population level, 64.5% of neurons (196/304) were classified as path-dependent (Pearson correlation coefficient $r\geq0.3$), while 35.5% (108/304) were classified as time-dependent (Pearson correlation coefficient $r<0.3$), highlighting substantial heterogeneity in temporal response organization within the ENTO. To determine how this temporal structure contributed to motion encoding, decoding analyses were performed (Figure 4G). Color information was extracted most efficiently, reaching 93.9%±4.2% accuracy in six-color classification with only 11 neurons (SVM). Shape information required a larger population, with 171 neurons needed to achieve 90.4%±1.9% accuracy in six-shape classification (SVM). Decoding of motion direction from mean firing rate yielded only moderate performance (63.2%±1.8%, SVM, eight directions), whereas accuracy increased sharply to 95%±1% when temporal response sequences were incorporated with an LSTM model ($n=60$). These results confirm that direction information in the ENTO is primarily encoded through the temporal structure of neuronal firing patterns.

Previous studies have identified time-to-collision (TTC) neurons in the ENTO region, including tau and eta neurons (Engelage & Bischof, 1996; Xiao et al., 2006). To define TTC-related coding more comprehensively, 217 neurons responsive to looming or fading stimuli were analyzed and grouped by K-means clustering according to firing pattern (Figure 4H). Among looming-responsive neurons, four distinct response types were resolved: Type 1 neurons (18.9%) exhibited a rapid firing rate increase at stimulus onset, followed by a gradual rise until collision; Type 2 neurons (16.6%) displayed firing dynamics consistent with eta neurons; Type 3 neurons (19.4%) exhibited tau-like firing patterns; and Type 4 neurons (45.2%) showed early peak firing prior to collision, followed by a slight decline and secondary rise near the collision point. Among fading-responsive neurons, four additional classes were identified: Type 1 neurons (39.2%) showed gradual decreases in firing rate as the object receded; Type 2 neurons (15.7%) exhibited increasing firing rates with object withdrawal; Type 3 neurons (36.9%) maintained high activity for an extended period before gradually decreasing to baseline; and Type 4 neurons (8.3%) were non-responsive to fading stimuli. These findings confirm the presence of canonical tau and eta neurons while revealing substantially greater diversity in TTC-related response dynamics within the ENTO.

Evidence for functional subdivisions in the ENTO

Spatial distribution of ENTO response properties was examined through analysis of inter-trial correlation and stimulus-specific consistency indices (Supplementary Figure S10). ITC captured trial-to-trial stability of firing patterns, providing a general measure of response reliability independent of any specific stimulus features. In contrast, consistency indices quantified the stability of neuronal preference for defined stimulus dimensions, including color, shape, and motion direction, across changing stimulus conditions. Together, these two metrics enabled separate assessment of general response reliability and feature-specific encoding fidelity.

For color stimuli, ITC exhibited significant spatial gradients along the AP (Pearson correlation coefficient $r=0.27$, $P<0.01$), ML (Pearson correlation coefficient $r=0.17$, $P<0.01$), and DV (Pearson correlation coefficient $r=0.20$, $P<0.01$) axes (Figure 5A, left panel). In parallel, neurons showing strong hue consistency were concentrated in the anteroventral-lateral ENTO (Figure 5A, right panel), supporting preferential engagement of this region in color processing. For shape stimuli, neither ITC nor orientation consistency showed a significant linear spatial gradient (Figure 5B). However, neurons with high ITC values were significantly clustered in the dorsal ENTO (DV>8.85, Mann-Whitney *U*-test, $P<0.01$),

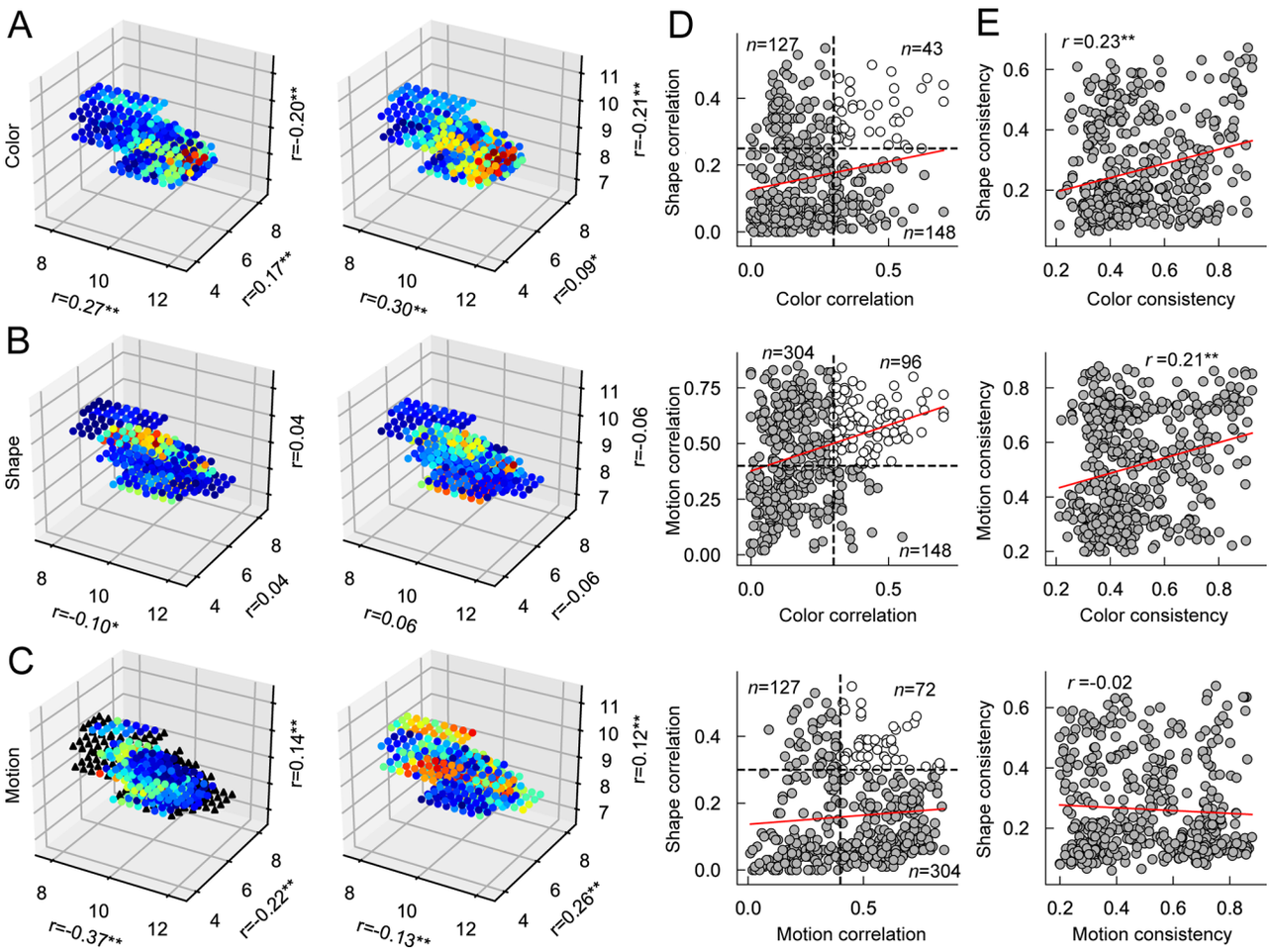

Figure 5 Spatial distribution and functional segregation of ENTO response properties

A: Spatial distribution of color response properties. Left panel: Spatial distribution of inter-trial correlations in the color paradigm. Linear correlations between inter-trial correlations and AP, ML, and DV positional values were calculated (Pearson correlation coefficient r, *: P<0.05; **: P<0.01). Right panel: Spatial distribution of hue consistency. B: Spatial distribution of shape response properties. Left panel: Inter-trial correlations in the shape paradigm. Right panel: Shape orientation consistency. C: Spatial distribution of motion response properties. Left panel: Motion energy in the motion receptive field paradigm. Right panel: Motion direction consistency. D: Distribution of high-reliability neurons. Top panel: Color vs. shape correlation (43 overlapping neurons). Middle panel: Color vs. motion correlation (96 overlapping neurons). Bottom panel: Motion vs. shape correlation (72 overlapping neurons). E: Comparison of color, shape, and motion consistency. Spearman correlation coefficient ρ, *: P<0.05; **: P<0.01, Color consistency: hue consistency. Shape consistency: orientation consistency. Motion consistency: direction consistency.

and orientation consistency was similarly enriched in dorsal regions (P<0.01). These findings indicate that shape processing is primarily localized to the dorsal ENTO. For motion stimuli, motion response energy was negatively correlated with the AP axis (Pearson correlation coefficient r=−0.37, P<0.01) and positively correlated with the ML axis (Pearson correlation coefficient r=0.22, P<0.01), suggesting that motion-sensitive neurons are predominantly located in the posterior-medial ENTO (Figure 5C, left panel). Although motion direction consistency showed only a weak correlation with the AP axis (Figure 5C, right panel, Pearson correlation coefficient r=0.13, P<0.01), Mann-Whitney U-test revealed significantly higher consistency in posterior than in anterior regions (AP boundary=10.57; P=0.019), suggesting that posterior ENTO neurons encode motion direction more reliably.

Functional segregation within the ENTO was further evaluated by quantifying neurons with high ITC values for color, shape, and motion stimuli. A total of 148 neurons (ITC>0.3) responded reliably to color stimuli, 127 neurons (ITC>0.25) to shape stimuli, and 304 neurons (ITC>0.4) to motion stimuli. Despite these sizable response populations, overlap between functional classes remained limited. Only 18.5% (43/232) of neurons were highly reliable for both color and shape (Figure 5D, top panel), 26.9% (96/356) for both color and motion (Figure 5D, middle panel), and 20.0% (72/359) for both motion and shape (Figure 5D, bottom panel). These distributions indicate that, despite some cross-domain convergence, most ENTO neurons are specialized for distinct stimulus domains. Correlation analysis of consistency indices supported this interpretation. Notably, color consistency showed weak but significant correlations with both shape consistency (Spearman correlation coefficient ρ=0.23) and motion consistency (Spearman correlation coefficient ρ=0.21), indicating partial convergence of color processing with other stimulus domains. In contrast, motion and shape consistency were not significantly correlated (Spearman correlation coefficient ρ=−0.02), suggesting that motion and shape encoding mechanisms remain functionally distinct within the ENTO (Figure 5E).

To determine whether these conjunctive response properties arise at the level of individual neurons or reflect

population-level activity, well-isolated units were separately analyzed (ISI violation rate<0.1%; Supplementary Figure S1A). Compared with MUA sites, these units showed no significant differences in most response measures but exhibited significantly higher tuning consistency for hue, shape, and motion direction (Supplementary Figure S1B), indicating more reliable feature encoding at the single-neuron level. Notably, a subset of single units showed overlapping selectivity across multiple features (Supplementary Figure S1C). Correlations in tuning consistency across domains were even stronger in single units, with Spearman correlation coefficients (ρ) of 0.60, 0.52, and 0.61 for color-shape, color-motion, and motion-shape, respectively (Supplementary Figure S1D). These findings confirm that conjunctive tuning in the ENTO exists at the level of individual neurons.

DISCUSSION

Understanding how birds perceive and recognize visual objects remains a fundamental question in neuroscience. One major issue is whether visual computation in birds follows principles shared with mammals or instead reflects a fundamentally distinct solution. Anatomical studies have identified the tectofugal pathway as the primary route for pattern recognition in birds, with visual signals processed hierarchically through the OT-RT-ENTO-MVL and NI-NCL circuits. However, the functional properties of these regions remain insufficiently defined. In the present study, ENTO neurons were examined electrophysiologically using controlled visual paradigms that varied across multiple stimulus dimensions, enabling fine-grained mapping of feature selectivity and spatial organization. The results showed that ENTO neurons were robustly responsive to color, shape, and motion, and that these response preferences were distributed nonrandomly along distinct anatomical axes, with color-dominant responses enriched anteroventrally, shape-related responses dorsally, and motion-related responses posteriorly (Figure 6). These results indicate that the ENTO exhibits a modular yet partially integrated architecture for encoding multidimensional visual information, supporting a central role in the avian visual hierarchy.

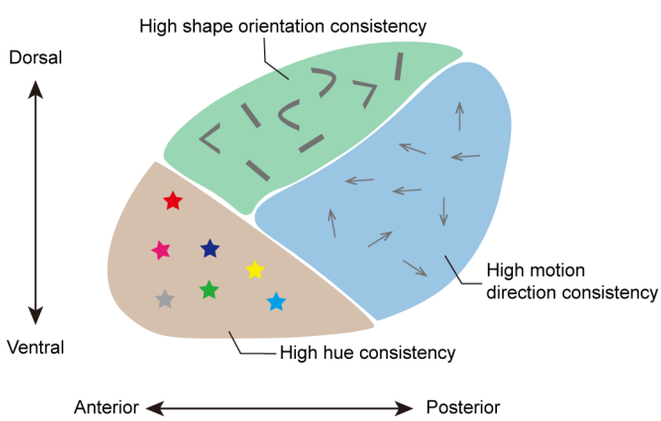

Figure 6 Regional organization of visual feature processing in pigeon entopallium

Different ENTO regions contained neurons showing higher consistency for specific visual features. Neurons in the anteroventral region showed more consistent responses to color (hue), those in the dorsal region responded more consistently to shape orientation, and those in the posterior region exhibited more consistent responses to motion direction.

The present findings both confirmed and extended previous understanding of ENTO physiology. In agreement with earlier studies (Gu et al., 2002; Xiao et al., 2006), ENTO neurons exhibited large receptive fields with circular, elliptical, or irregular geometries and, in some cases, localized response hotspots (Figure 1A). Additional analyses revealed pronounced spatial heterogeneity, with anterior neurons displaying larger ON receptive fields, ventral neurons exhibiting higher ON-OFF overlap (Figure 1F), and a subset of neurons lacking OFF responses also showing no sensitivity to motion (Supplementary Figure S10A). In the motion domain, the ENTO contained neurons with clear directional tuning, including biases toward forward and downward movement, consistent with previous reports (Gu et al., 2002; Kimberly et al., 1971; Xiao et al., 2006), as well as a large population of time-dependent neurons that enhanced motion decoding through temporal dynamics (Figure 4F, G). Analyses also confirmed the presence of tau and eta neurons (Engelage & Bischof, 1996; Wang et al., 1993; Xiao et al., 2006) and extended earlier classifications through clustering-based definition of TTC response profiles (Figure 4H). Critically, the present study provides the first detailed characterization of ENTO responses to color and shape, revealing luminance-invariant hue tuning (Figure 2F) together with strong orientation selectivity and more moderate angle and curvature sensitivity (Figure 3D–F).

Relative to mammalian visual areas, the ENTO exhibits a distinctive combination of broad receptive fields and multidimensional feature coding. ENTO receptive fields were substantially larger (101.6°; Figure 1D) than those reported for the primate V4 region (4–6°) (Kastner et al., 2001), exceeded the range commonly observed in the middle temporal visual area (MT, 5–50°) (Albright & Desimone, 1987; Lui & Rosa, 2015), and approached values described for the IT (Smith et al., 2001). This receptive field scale indicates a capacity for broad spatial integration and is likely advantageous for detecting behaviorally relevant motion over wide regions of visual space. In the color domain, ENTO neurons exhibited luminance-invariant hue tuning (Figure 2F), a property reminiscent of color-selective domains in primate V4 (Conway et al., 2007). A pronounced end-spectral bias was also evident, with stronger responses to red hues (Figure 2H, I), consistent with reports from non-human primates (Liu et al., 2020; Purdy, 1931; Yoshioka et al., 1996) and humans (Nasr & Tootell, 2018) across both early and higher-order visual regions. Red stimuli have also been shown to evoke stronger gamma oscillations in macaque V1 (Shirhatti & Ray, 2018), with recent work in pigeons similarly identifying gamma-band responses to hue differences in the ENTO (Niu et al., 2024), suggesting dynamic spectral encoding in both species. In the domain of shape processing (Figure 3), ENTO neurons exhibited partial orientation invariance but weaker selectivity for curvature and angle than the highly specialized shape representations reported for primate V4 (Hegdé & Van Essen, 2007; Jiang et al., 2021; Pasupathy & Connor, 1999). Taken together, these findings indicate that pigeon ENTO supports robust multidimensional visual processing within a single anatomical region. Large receptive fields, functional heterogeneity, and spatially organized feature maps indicate that the ENTO serves as a convergence hub for integrating visual features, performing functions that are partitioned across multiple cortical regions in primates. This compact yet

versatile architecture may reflect a distinct, but convergent, evolutionary strategy for intermediate-level visual processing in birds.

Traditional frameworks have proposed that the avian visual wulst corresponds functionally to the mammalian dorsal visual stream, with primary roles in spatial localization and direction analysis, whereas the ENTO parallels the ventral stream and supports object recognition (Goodale & Milner, 1992; Riesenhuber & Poggio, 1999; Ungerleider & Haxby, 1994; Watanabe et al., 2011). However, the present findings challenge this strict functional dichotomy. Notably, results showed that ENTO neurons encoded not only static features such as color and shape (Figure 2, 3), which are classically associated with "what" processing, but also dynamic features such as motion direction (Figure 4). Furthermore, color and shape information remained decodable during motion processing (Figure 4D, E). One plausible interpretation is that the ENTO contributes to recognition of moving objects, potentially supporting target identification during ecologically relevant behaviors such as prey capture or predator avoidance. A comparable integration of stimulus features has been reported in primate V4. Although traditionally classified within the ventral stream, the V4 region contains direction-selective neurons (Li et al., 2025), exhibits systematic maps of motion preference (Li et al., 2013), and responds to kinetic boundaries (Mysore et al., 2006). Additionally, V4 also contains locally clustered domains preferentially sensitive to color (globs) and shape (interglobs) (Conway et al., 2007; Tanigawa et al., 2010), and some neurons show combined sensitivity to both dimensions (Garg et al., 2019). These observations closely parallel the functional arrangement identified in the avian ENTO (Figure 5D, E). Although the ENTO shares with the mammalian ventral stream a major role in object-related processing, its capacity to encode motion suggests a more integrative, hybrid strategy. This may represent an evolutionary adaptation in birds, allowing the ENTO to support both object recognition and motion-based target tracking within a single visual hub.

The present study defined receptive field properties and functional organization in pigeon ENTO using electrophysiological recordings under anesthesia. Although anesthesia reduces behavioral confounds, the extent to which it preserves native neural dynamics remains unresolved. Some studies have reported preservation of tuning properties under anesthesia (Shevelev et al., 1990; Wang et al., 2013), while others have documented alterations in spontaneous activity and information processing (Goltstein et al., 2015). Direct characterization of ENTO responses in awake states therefore remains a crucial area for future investigation. In addition, all recordings in this study were obtained from the left ENTO. However, previous studies have demonstrated pronounced hemispheric lateralization within the avian tectofugal visual pathway (Pusch et al., 2023). Specifically, the left hemisphere, which receives input from the right eye, has been linked to fine perceptual discrimination, category learning, and local feature analysis (Güntürkün, 1985; Rogers et al., 2007; Skiba et al., 2002), whereas the right hemisphere, which receives input from the left eye, has been associated with global integration, spatial processing, and rapid response control (Rugani et al., 2015; Yamazaki et al., 2007). As such, the present focus on the left ENTO provides valuable insight into category-related processing but may underestimate contributions from the right ENTO to motion integration or global feature processing. Although the current results establish a foundation for understanding ENTO feature representations and functional subdivisions, the precise contribution of this region to object recognition remains unclear. Conventional artificial stimuli provide experimental control but do not fully capture the complexity of natural visual environments, thereby limiting inference regarding real-world visual processing. Recent advances in computational neuroscience, including neuronal response modeling and generative approaches (Hatanaka et al., 2022; Wang et al., 2024; Yamins et al., 2014), offer promising strategies to bridge this gap by identifying optimal stimulus features from large-scale natural image datasets. Future work combining naturalistic stimuli, large-scale recordings, and awake-state preparations will be critical for uncovering the full contribution of the ENTO to complex visual processing.

DATA AVAILABILITY

The data that support the findings of this study are available in the following repository: https://doi.org/10.6084/m9.figshare.28615325. Source data are provided with this paper.

SUPPLEMENTARY DATA

Supplementary data to this article can be found online.

COMPETING INTERESTS

The authors declare that they have no competing interests.

AUTHORS' CONTRIBUTIONS

J.C.Z., M.J.Z., and Z.Z.W. conceived and designed the study. J.C.Z. and Q.Z.H. performed the surgery and experiments. J.C.Z., X.K.N., and J.T.W. analyzed the data. P.W. developed the visual stimulus procedure. J.C.Z., M.J.Z., and Z.Z.W. wrote the manuscript. All authors read and approved the final version of the manuscript.

REFERENCES

Albright TD, Desimone R. 1987. Local precision of visuotopic organization in the middle temporal area (MT) of the macaque. *Experimental Brain Research*, **65**(3): 582–592.

Anderson C, Parra RS, Chapman H, et al. 2020b. Pigeon nidopallium caudolaterale, entopallium, and mesopallium ventrolaterale neural responses during categorisation of Monet and Picasso paintings. *Scientific Reports*, **10**(1): 15971.

Anderson C, Johnston M, Marrs EJ, et al. 2020a. Delay activity in the Wulst of pigeons (*Columba livia*) represents correlates of both sample and reward information. *Neurobiology of Learning and Memory*, **171**: 107214.

Azizi AH, Pusch R, Koenen C, et al. 2019. Emerging category representation in the visual forebrain hierarchy of pigeons (*Columba livia*). *Behavioural Brain Research*, **356**: 423–434.

Benowitz LI, Karten HJ. 1976. Organization of the tectofugal visual pathway in the pigeon: a retrograde transport study. *Journal of Comparative Neurology*, **167**(4): 503–520.

Bessette BB, Hodos W. 1989. Intensity, color, and pattern discrimination deficits after lesions of the core and belt regions of the ectostriatum. *Visual Neuroscience*, **2**(1): 27–34.

Clark W, Chilcott M, Azizi A, et al. 2022. Neurons in the pigeon visual network discriminate between faces, scrambled faces, and sine grating images. *Scientific Reports*, **12**(1): 589.

Conway BR, Moeller S, Tsao DY. 2007. Specialized color modules in macaque extrastriate cortex. *Neuron*, **56**(3): 560–573.

Cook RG, Patton TB, Shimizu T. 2013. Functional segregation of the Entopallium in pigeons. *Philosophy*, **130**: 59–86.

Deng C, Rogers LJ. 1998. Bilaterally projecting neurons in the two visual

pathways of chicks. *Brain Research*, **794**(2): 281–290.
Dill LM. 1974. The escape response of the zebra danio (*Brachydanio rerio*) I. The stimulus for escape. *Animal Behaviour*, **22**(3): 711–722.
Engelage J, Bischof HJ. 1996. Single-cell responses in the ectostriatum of the zebra finch. *Journal of Comparative Physiology A*, **179**(6): 785–795.
Garcia CD, Liu S, Laurens J, et al. 2018. Neuronal thresholds and correlations in the peripheral vestibular system during rotation discrimination. *BioRxiv*, doi: https://doi.org/10.1101/343764.
Garg AK, Li PC, Rashid MS, et al. 2019. Color and orientation are jointly coded and spatially organized in primate primary visual cortex. *Science*, **364**(6447): 1275–1279.
Goltstein PM, Montijn JS, Pennartz CMA. 2015. Effects of isoflurane anesthesia on ensemble patterns of Ca^{2+} activity in mouse V1: reduced direction selectivity independent of increased correlations in cellular activity. *PLoS One*, **10**(2): e0118277.
Goodale MA, Milner AD. 1992. Separate visual pathways for perception and action. *Trends in Neurosciences*, **15**(1): 20–25.
Gu Y, Wang Y, Zhang T, et al. 2002. Stimulus size selectivity and receptive field organization of ectostriatal neurons in the pigeon. *Journal of Comparative Physiology A*, **188**(3): 173–178.
Güntürkün O. 1985. Lateralization of visually controlled behavior in pigeons. *Physiology & Behavior*, **34**(4): 575–577.
Halpern BP, Karten HJ, Hodos W. 1968. A stereotaxic atlas of the brain of the pigeon (*Columba livia*). *American Journal of Psychology*, **81**(2): 289.
Hatanaka G, Inagakai M, Takeuchi RF, et al. 2022. Processing of visual statistics of naturalistic videos in macaque visual areas V1 and V4. *Brain Structure and Function*, **227**(4): 1385–1403.
Hegdé J, Van Essen DC. 2007. A comparative study of shape representation in macaque visual areas V2 and V4. *Cerebral Cortex*, **17**(5): 1100–1116.
Hellmann B, Güntürkün O. 2001. Structural organization of parallel information processing within the tectofugal visual system of the pigeon. *Journal of Comparative Neurology*, **429**(1): 94–112.
Hunt SP, Künzle H. 1976. Observations on the projections and intrinsic organization of the pigeon optic tectum: an autoradiographic study based on anterograde and retrograde, axonal and dendritic flow. *Journal of Comparative Neurology*, **170**(2): 153–172.
Husband SA, Shimizu T. 1999. Efferent projections of the ectostriatum in the pigeon (*Columba livia*). *Journal of Comparative Neurology*, **406**(3): 329–345.
Jiang RD, Andolina IM, Li M, et al. 2021. Clustered functional domains for curves and corners in cortical area V4. *eLife*, **10**: e63798.
Johnston M, Anderson C, Colombo M. 2017. Pigeon NCL and NFL neuronal activity represents neural correlates of the sample. *Behavioral Neuroscience*, **131**(3): 213–219.
Karten HJ, Hodos W. 1970. Telencephalic projections of the nucleus rotundus in the pigeon (*Columba livia*). *Journal of Comparative Neurology*, **140**(1): 35–51.
Karten HJ. 2015. Vertebrate brains and evolutionary connectomics: on the origins of the mammalian 'neocortex'. *Philosophical Transactions of the Royal Society B: Biological Sciences*, **370**(1684): 20150060.
Kastner S, De Weerd P, Pinsk MA, et al. 2001. Modulation of sensory suppression: implications for receptive field sizes in the human visual cortex. *Journal of Neurophysiology*, **86**(3): 1398–1411.
Kimberly RP, Holden AL, Bamborough P. 1971. Response characteristics of pigeon forebrain cells to visual stimulation. *Vision Research*, **11**(5): 475–478.
Krützfeldt NOE, Wild JM. 2005. Definition and novel connections of the entopallium in the pigeon (*Columba livia*). *Journal of Comparative Neurology*, **490**(1): 40–56.
Levenson RM, Krupinski EA, Navarro VM, et al. 2015. Pigeons (*Columba livia*) as trainable observers of pathology and radiology breast cancer images. *PLoS One*, **10**(11): e0141357.
Li PC, Ma H, Lu HD. 2025. Direction-selective neurons in macaque V4. *Journal of Neurophysiology*, **133**(5): 1572–1582.
Li PC, Zhu SD, Chen M, et al. 2013. A motion direction preference map in monkey V4. *Neuron*, **78**(2): 376–388.
Liu RL, Wang K, Meng JJ, et al. 2013. Adaptation to visual stimulation modifies the burst firing property of V1 neurons. *Zoological Research*, **34**(E3): 245101.
Liu Y, Li M, Zhang X, et al. 2020. Hierarchical representation for chromatic processing across macaque V1, V2, and V4. *Neuron*, **108**(3): 538–550. e5.
Lui LL, Rosa MGP. 2015. Structure and function of the middle temporal visual area (MT) in the marmoset: comparisons with the macaque monkey. *Neuroscience Research*, **93**: 62–71.
Majaj NJ, Hong H, Solomon EA, et al. 2015. Simple learned weighted sums of inferior temporal neuronal firing rates accurately predict human core object recognition performance. *Journal of Neuroscience*, **35**(39): 13402–13418.
Mysore SG, Vogels R, Raiguel SE, et al. 2006. Processing of kinetic boundaries in macaque V4. *Journal of Neurophysiology*, **95**(3): 1864–1880.
Nasr S, Tootell RBH. 2018. Columnar organization of mid-spectral and end-spectral hue preferences in human visual cortex. *Neuroimage*, **181**: 748–759.
Navarro VM, Wasserman EA, Slomka P. 2020. Taking pigeons to heart: birds proficiently diagnose human cardiac disease. *Learning & Behavior*, **48**(1): 9–21.
Nguyen AP, Spetch ML, Crowder NA, et al. 2004. A dissociation of motion and spatial-pattern vision in the avian telencephalon: implications for the evolution of "visual streams". *Journal of Neuroscience*, **24**(21): 4962–4970.
Niu XK, Peng YY, Jiang ZY, et al. 2024. Gamma-band-based dynamic functional connectivity in pigeon entopallium during sample presentation in a delayed color matching task. *Cognitive Neurodynamics*, **18**(1): 37–47.
Nixdorf BE, Bischof HJ. 1982. Afferent connections of the ectostriatum and visual Wulst in the zebra finch (*Taeniopygia guttata castanotis Gould*)–an HRP study. *Brain Research*, **248**(1): 9–17.
Oghazian M, Saffari F, Khadem A. 2021. Discrimination between inhibitory and excitatory neurons of mouse hippocampus based on the shape of extracellular spike waveforms. *Frontiers in Biomedical Technologies*, **8**(3): 161–169.
Orban GA, Kennedy H, Bullier J. 1986. Velocity sensitivity and direction selectivity of neurons in areas V1 and V2 of the monkey: influence of eccentricity. *Journal of Neurophysiology*, **56**(2): 462–480.
Pasupathy A, Connor CE. 1999. Responses to contour features in macaque area V4. *Journal of Neurophysiology*, **82**(5): 2490–2502.
Pepperberg IM, Nakayama K. 2016. Robust representation of shape in a Grey parrot (*Psittacus erithacus*). *Cognition*, **153**: 146–160.
Purdy DM. 1931. On the saturations and chromatic thresholds of the spectral colours. *British Journal of Psychology*. *General Section*, **21**(3): 283–313.
Pusch R, Clark W, Rose J, et al. 2023. Visual categories and concepts in the avian brain. *Animal Cognition*, **26**(1): 153–173.
Pusch R, Packheiser J, Koenen C, et al. 2022. Digital embryos: a novel technical approach to investigate perceptual categorization in pigeons (*Columba livia*) using machine learning. *Animal Cognition*, **25**(4): 793–805.
Qadri MAJ, Cook RG. 2017. Pigeons and humans use action and pose information to categorize complex human behaviors. *Vision Research*, **131**: 16–25.
Quiroga RQ, Nadasdy Z, Ben-Shaul Y. 2004. Unsupervised spike detection and sorting with wavelets and superparamagnetic clustering. *Neural Computation*, **16**(8): 1661–1687.
Revzin AM, Karten H. 1967. Rostral projections of the optic tectum and the

nucleus rotundus in the pigeon. *Brain Research*, **3**(3): 264–276.
Riesenhuber M, Poggio T. 1999. Hierarchical models of object recognition in cortex. *Nature Neuroscience*, **2**(11): 1019–1025.
Rogers LJ, Andrew RJ, Johnston ANB. 2007. Light experience and the development of behavioural lateralization in chicks: III. Learning to distinguish pebbles from grains. *Behavioural Brain Research*, **177**(1): 61–69.
Rugani R, Salva OR, Regolin L, et al. 2015. Brain asymmetry modulates perception of biological motion in newborn chicks (*Gallus gallus*). *Behavioural Brain Research*, **290**: 1–7.
Scarf D, Hayne H, Colombo M. 2011. Pigeons on par with primates in numerical competence. *Science*, **334**(6063): 1664–1664.
Shanahan M, Bingman VP, Shimizu T, et al. 2013. Large-scale network organization in the avian forebrain: a connectivity matrix and theoretical analysis. *Frontiers in Computational Neuroscience*, **7**: 89.
Shevelev IA, Lazareva NA, Novikova RV, et al. 1990. Dynamics of orientational tuning of feling visual cortex neurons under the effects of sombrevine. *Neurophysiology*, **22**(1): 89–94.
Shimizu T, Bowers AN. 1999. Visual circuits of the avian telencephalon: evolutionary implications. *Behavioural Brain Research*, **98**(2): 183–191.
Shirhatti V, Ray S. 2018. Long-wavelength (reddish) hues induce unusually large gamma oscillations in the primate primary visual cortex. *Proceedings of the National Academy of Sciences of the United States of America*, **115**(17): 4489–4494.
Skiba M, Diekamp B, Güntürkün O. 2002. Embryonic light stimulation induces different asymmetries in visuoperceptual and visuomotor pathways of pigeons. *Behavioural Brain Research*, **134**(1-2): 149–156.
Smith AT, Singh KD, Williams AL, et al. 2001. Estimating receptive field size from fMRI data in human striate and extrastriate visual cortex. *Cerebral Cortex*, **11**(12): 1182–1190.
Soto FA, Wasserman EA. 2016. Promoting rotational-invariance in object recognition despite experience with only a single view. *Behavioural Processes*, **123**: 107–113.
Tanigawa H, Lu HD, Roe AW. 2010. Functional organization for color and orientation in macaque V4. *Nature Neuroscience*, **13**(12): 1542–1548.
Ungerleider LG, Haxby JV. 1994. 'What' and 'where' in the human brain. *Current Opinion in Neurobiology*, **4**(2): 157–165.
Vincent JP, Economo MN. 2024. Assessing cross-contamination in spike-sorted electrophysiology data. *eNeuro*, **11**(8): ENEURO.0554–23.2024.
Wang K, Zhu H, Chen CY, et al. 2013. Effects of ketamine and urethane on stimulation-induced c-fos expression in neurons of cat visual cortex. *Zoological Research*, **34**(6): 582–588.
Wang TY, Lee TS, Yao HX, et al. 2024. Large-scale calcium imaging reveals a systematic V4 map for encoding natural scenes. *Nature Communications*, **15**(1): 6401.
Wang YC, Jiang SY, Frost BJ. 1993. Visual processing in pigeon nucleus rotundus: luminance, color, motion, and looming subdivisions. *Visual Neuroscience*, **10**(1): 21–30.
Watanabe S. 1991. Effects of ectostriatal lesions on natural concept, pseudoconcept, and artificial pattern discrimination in pigeons. *Visual Neuroscience*, **6**(5): 497–506.
Watanabe S. 1994. Experimental visual agnosia in the pigeon. *Brazilian Journal of Medical and Biological Research*, **27**(3): 563–571.
Watanabe S. 2003. Effects of Wulst and ectostriatum lesions on repeated acquisition of spatial discrimination in pigeons. *Cognitive Brain Research*, **17**(2): 286–292.
Watanabe S, Mayer U, Bischof HJ. 2011. Visual Wulst analyses "where" and entopallium analyses "what" in the zebra finch visual system. *Behavioural Brain Research*, **222**(1): 51–56.
Xiao Q, Li DP, Wang SR. 2006. Looming-sensitive responses and receptive field organization of telencephalic neurons in the pigeon. *Brain Research Bulletin*, **68**(5): 322–328.
Yamazaki Y, Aust U, Huber L, et al. 2007. Lateralized cognition: asymmetrical and complementary strategies of pigeons during discrimination of the "human concept". *Cognition*, **104**(2): 315–344.
Yamins DLK, Hong H, Cadieu CF, et al. 2014. Performance-optimized hierarchical models predict neural responses in higher visual cortex. *Proceedings of the National Academy of Sciences of the United States of America*, **111**(23): 8619–8624.
Yoshida T, Ohki K. 2020. Natural images are reliably represented by sparse and variable populations of neurons in visual cortex. *Nature Communications*, **11**(1): 872.
Yoshioka T, Dow BM, Vautin RG. 1996. Neuronal mechanisms of color categorization in areas V1, V2 and V4 of macaque monkey visual cortex. *Behavioural Brain Research*, **76**(1-2): 51–70.
Zoccolan D, Kouh M, Poggio T, et al. 2007. Trade-off between object selectivity and tolerance in monkey inferotemporal cortex. *Journal of Neuroscience*, **27**(45): 12292–12307.